

# High Specific Surface Area Activated Carbon with Well-Balanced Micro/Mesoporosity for Ultrahigh Supercapacitive Performance

Bo Hou, Tong Zhang, Rongwei Yan, De Li, Yan Mo, Lihong Yin, Yong Chen\*

State Key Laboratory of South China Sea Marine Resource Utilisation, Hainan Provincial Key Laboratory of Research on Utilization of Si-Zr-Ti Resources, Hainan University, 570228 Haikou, China

\*E-mail: [ychen2002@163.com](mailto:ychen2002@163.com)

Received: 15 July 2016 / Accepted: 10 September 2016 / Published: 10 October 2016

---

High specific surface area activated carbon derived from coconut shell was prepared using low-temperature carbonization followed by KOH activation method. The resulting activated carbon exhibited excellent supercapacitance performance with an obtained specific capacitance of 325 F g<sup>-1</sup> at 0.1 A g<sup>-1</sup>. Moreover, the supercapacitor electrodes retained 71% of the initial capacitance at elevated current densities of 100 A g<sup>-1</sup> and 89% after 10000 cycles when tested in 6 M KOH aqueous solution. Also, the equivalent series resistance of the system was recorded to be only 0.36 Ω. Meanwhile, testing of the supercapacitor electrodes in ionic liquid based-electrolyte delivered substantial specific capacitance of 198 F g<sup>-1</sup> and an ultrahigh power density of 74.2 kW kg<sup>-1</sup>.

---

**Keywords:** Coconut shell; Supercapacitors; Pore size distribution; Power density

## 1. INTRODUCTION

As the fossil energy is being depleted and air pollution became more and more a serious issue, renewable and environmentally friendly energy storage devices gained increased demand as alternative energy sources [1-3]. Currently, supercapacitors are widely utilized in consumer electronics, industrial power, and hybrid or full electric vehicles. This is due to their long cycle life, high power density, increased safety, and environmental friendliness [1, 4]. However, their relatively low energy density limits their further application in modern society. Therefore, tremendous efforts were made to enhance their energy density without affecting their large power density.

The energy storage of the electrical double layer capacitors (EDLC) relies on electrostatic adsorption at the electrode/electrolyte interface. Hence, both the specific surface area (SSA) and the pore size distribution (PSD) are essential in the performance of electrode materials [5, 6]. It has been demonstrated that pore size less than 1 nm may obviously enhance the specific capacitance, whereas micropore size smaller than 0.5 nm is insufficient to form a double layer [7, 8]. The suitable pore size should be slightly larger than the ion size of the electrolyte [7-9]. Also, it was found that mesopores could promote electrolyte diffusion, leading to improvement in the power density [10-12]. Hence, it might be speculated that hierarchically porous carbon could lead to better supercapacitive performances [11].

Traditionally, coconut shells were used as raw materials for preparation of activated carbon (AC) for supercapacitors, due to their unique natural structure, high carbon content and low ash content [13-17]. It has been demonstrated that the capacitance performance is dependent on the PSD and SSA of the AC, as well as the preparation method. A good performance was achieved with activated carbon synthesized using one-step thermal treatment method but suffered from poor cycle stability [16]. A high rate performance was obtained with sheet-like graphitic carbon through complicated synthetic route in the presence of additional catalyst [15]. With respect to coconut shell based activated carbon, though several reports have been published, the optimal preparation technology is still not fully development and is being further explored.

This account is devoted to the synthesis of activated carbon with improved capacitive properties from coconut shells through low-temperature carbonization and KOH activation process. The AC sample with a high SSA ( $3512.83 \text{ m}^2 \text{ g}^{-1}$ ), well-balanced micro/mesoporosity (39.3%) and large pore volume ( $2.11 \text{ cm}^3 \text{ g}^{-1}$ ) was obtained by using optimal preparation parameter. The AC delivers the high specific capacity up to  $325 \text{ F g}^{-1}$  at  $0.1 \text{ A g}^{-1}$  and 71% capacitance retention at  $100 \text{ A g}^{-1}$  in 6 M KOH aqueous solution, respectively. Moreover, the ultrahigh power density of  $74.2 \text{ kW kg}^{-1}$  was achieved at an energy density of  $46.6 \text{ Wh kg}^{-1}$  in ionic liquid electrolyte.

## 2. EXPERIMENTAL

### 2.1 Preparation of ACs

Fig. 1 shows the AC preparation process, where the coconut shell powder was first pyrolyzed at  $350 \text{ }^\circ\text{C}$  for 2 h under nitrogen environment. It was then mixed with KOH and subsequently activated at  $300 \text{ }^\circ\text{C}$  then  $750 \text{ }^\circ\text{C}$  for periods of 1 h each at a heating rate of  $10 \text{ }^\circ\text{C min}^{-1}$ . Next, the product was washed with water until pH became neutral and subsequent dried at  $110 \text{ }^\circ\text{C}$ . The AC samples were denoted as AC-X, where X corresponds to the weight ratio of KOH/C.

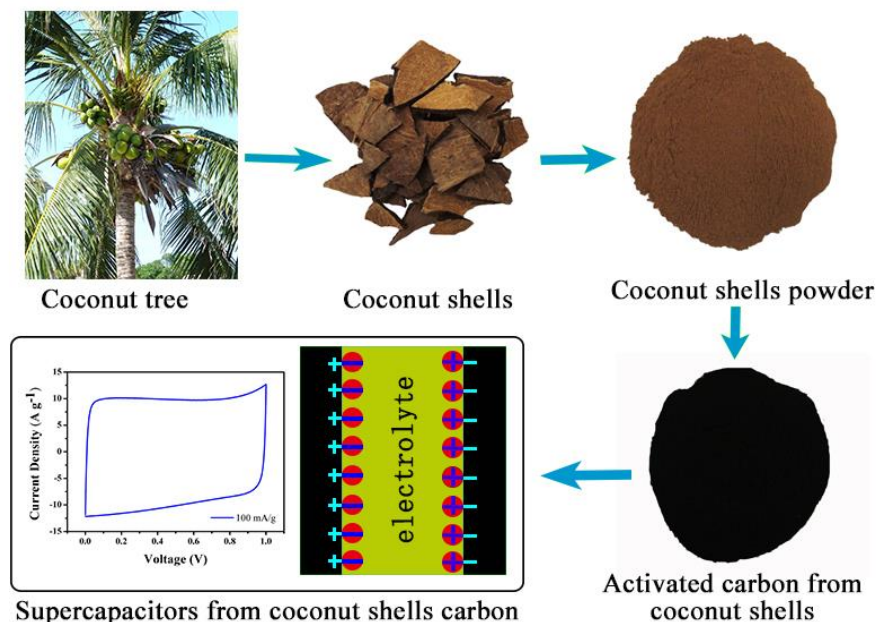


**Figure 1.** Schematic diagram of the AC preparation process.

## 2.2 Characterization

X-ray diffraction (XRD) patterns were obtained with a Bruker D8 Advance diffractometer with Cu K $\alpha$  radiation. The Raman spectra were recorded on a Renishaw InVia Raman Microscope at laser source wavelength of 514 nm. X-ray photoelectron spectrometer (XPS, Thermo Fisher Escalab 250Xi) was used for the surface analysis of the ACs. The dynamic water contact angle measurements were acquired by an SPCA contact angle measurement system. The nitrogen adsorption-desorption isotherms were recorded at  $-196^{\circ}\text{C}$  at a relative pressure of  $P/P_0 = 0.989$  on a JW-BK132F system. The SSA was determined by Brunauer-Emmett-Teller (BET) method. The pore volumes were analyzed by the Barrett-Joyner-Halenda for mesopores and Horvath-Kawazoe methods for micropores. The PSD was computed using a non-local density functional theory method.

## 2.3 Electrochemical Measurements

The AC was first mixed with Ketjen black and polytetrafluoroethylene at a weight ratio of 80:15:5, respectively. The mixture was then pasted and pressed onto nickel foam at 10 MPa. After drying at  $110^{\circ}\text{C}$  for 12 h under vacuum, two electrodes with diameters of 10 mm were assembled in a CR2025 coin cell separated by glass microfibrer (Whatman) filled with either aqueous solution or ionic liquid electrolyte.

The electrochemical impedance spectroscopy (EIS) and cyclic voltammetry (CV) were recorded by a Bio-logic VSP-300 electrochemical workstation. Galvanostatic charge-discharge (GCD) was performed on a battery test system (CT2001A LAND). EIS was collected in the frequency range from 10 mHz to 100 kHz with  $\pm 5$  mV voltage amplitude. The working voltage windows were set to 0-

1.0 V for 6 M KOH and 0-3.5 V for 1-ethyl-3-methylimidazolium tetrafluoroborate (EMIMBF<sub>4</sub>, Sigma-Aldrich) electrolytes, respectively.

The specific capacitance ( $C$ , F g<sup>-1</sup>) was estimated from CV curves using Eq. (1):

$$C = \frac{\int i \cdot dV}{\nu m V} \quad (1)$$

where  $i$ ,  $\nu$ ,  $m$  and  $V$  are the instant current (A), scan rate (V s<sup>-1</sup>), the AC mass load (g) and the voltage window (V), respectively.

The specific capacitance ( $C_s$ , F g<sup>-1</sup>) was calculated from GCD curve using Eq. (2) [18]:

$$C_s = \frac{2 \times I_{cons} \times \Delta t}{m \times \Delta V} \quad (2)$$

where  $I_{cons}$  (A) is the current,  $\Delta t$  (s) is the discharge time,  $m$  (g) represents the active mass of the material on one electrode, and  $\Delta V$  (V) is the voltage window during a discharge cycle (excluding the IR drop).

The energy density ( $E$ , Wh kg<sup>-1</sup>) of the cell was obtained by Eq. (3):

$$E = \frac{C_s \times V_{max}^2}{2 \times 4 \times 3.6} \quad (3)$$

where  $V_{max}$  is the estimated cell voltage after the IR drop.

The power density ( $P$ , W kg<sup>-1</sup>) of the cell was calculated by Eq. (4):

$$P = \frac{E \times 3600}{\Delta t} \quad (4)$$

### 3. RESULTS AND DISCUSSION

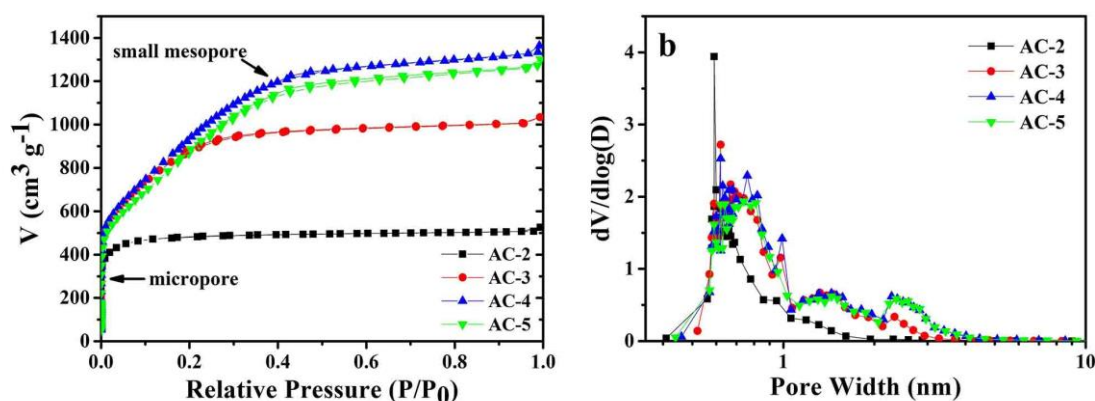


**Figure 2.** (a) The nitrogen adsorption-desorption isotherms of ACs. (b) The PSD curves of ACs.

The nitrogen adsorption-desorption data of Fig. 2a revealed that unlike other samples, AC-2 showed a type-I isotherm that implies a structure formed mostly by micropores [19]. The other isotherms, however, exhibited a linear multilayer adsorption characteristic of mesopores [20]. The detailed specific surface area and pore volume are listed in Table 1. It can be seen that both SSA and

pore volume increased gradually as X rose from 2 to 4, then declined when X reached 5, indicating the production of more mesopores as KOH increased [6]. The recorded maximum values of SSA and pore volume were 3512.83 m<sup>2</sup> g<sup>-1</sup> and 2.11 cm<sup>3</sup> g<sup>-1</sup> for X=4, respectively. The PSD curves of Fig. 2b depicted that all samples have a substantial number of mesopores with sizes ranging from 2-3 nm, except for sample AC-2.

**Table 1.** SSA and pore volume values of all prepared AC samples

Sample	S <sub>BET</sub> (m <sup>2</sup> g <sup>-1</sup> )	V <sub>total</sub> (cm <sup>3</sup> g <sup>-1</sup> )	V <sub>micro</sub> (cm <sup>3</sup> g <sup>-1</sup> )	V <sub>mes</sub> /V <sub>total</sub> (%)
AC-2	1878.89	0.81	0.73	9.9
AC-3	3106.44	1.60	1.22	23.8
AC-4	3512.83	2.11	1.28	39.3
AC-5	3313.27	2.01	1.15	42.8

S<sub>BET</sub>: BET specific surface area; V<sub>total</sub>: Total pore volume; V<sub>micro</sub>: Micropore volume; V<sub>mes</sub>: Mesopore volume.

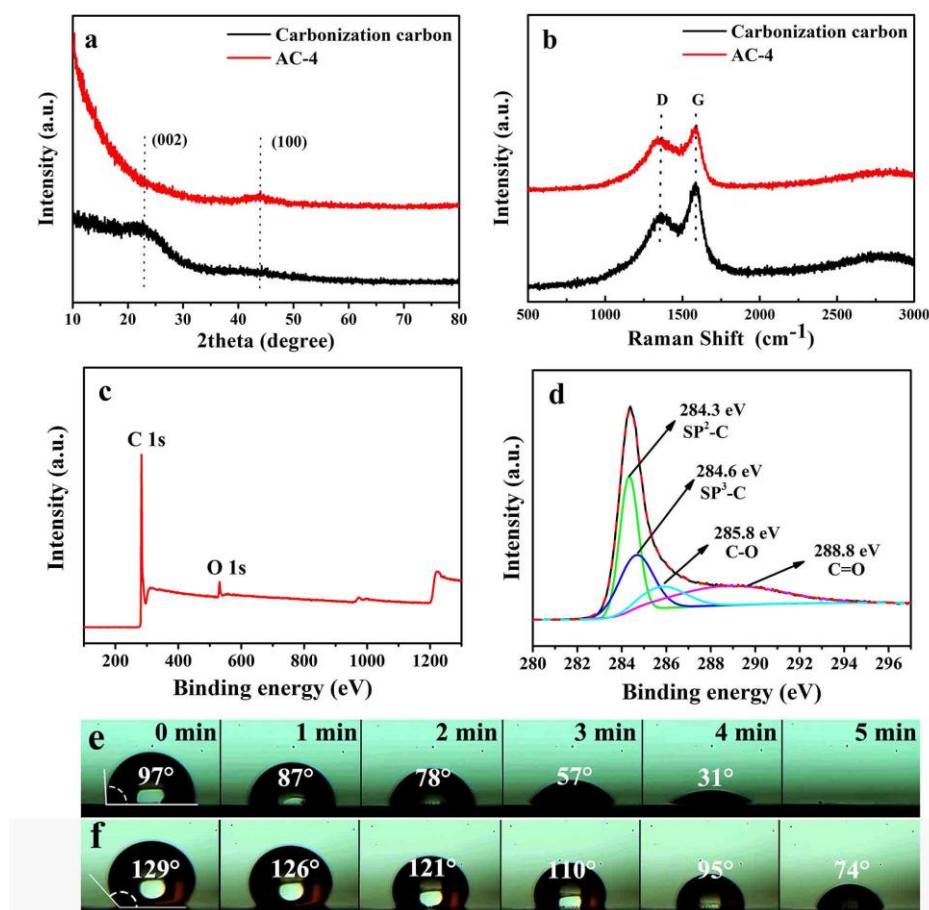


**Figure 3.** (a) XRD curves of sample AC-4 in comparison with carbonized carbon. (b) Raman spectra of sample AC-4 in comparison with carbonized carbon. (c) XPS spectra of AC-4, and the high-resolution spectra of C<sub>1s</sub> peak (d). Dynamic water contact angle of AC-4 (e) and commercial AC (f).

The XRD patterns of AC-4 in comparison with carbon carbonized at 350 °C are shown in Fig. 3a. Two broad peaks located at  $2\theta$  of 22.7° and 44° assigned to the (002) and (100) planes of carbon were recorded. While the (002) peak of AC-4 sample looked indistinct, the intensity of the (100) peak significantly increased, suggesting that the carbon structure suffered destruction during the KOH-activation process. The Raman spectra of Fig. 3b showed two clear peaks at 1358  $\text{cm}^{-1}$  (D-band) and 1584  $\text{cm}^{-1}$  (G-band), corresponding to the defected carbon and the crystallites graphite, respectively [21]. The intensity ratio ( $I_D/I_G$ ) is proportional to the crystalline degree of carbon [22]. The estimated  $I_D/I_G$  values of carbonization carbon and AC-4 were 0.78 and 0.85, respectively. The elevated value of AC-4 was attributed to the severe damage of graphite crystallite caused by KOH etching process that resulted in increased disorder of carbon [23]. In addition, the XPS results of Fig. 3c revealed that the AC-4 sample contained only carbon (95.76%) and oxygen (4.24%). The high-resolution  $\text{C}_{1s}$  spectra shown in Fig. 3d might be deconvoluted into four peaks, consisting of  $\text{sp}^2$ -bonded carbon (284.3 eV),  $\text{sp}^3$ -bonded carbon (284.6 eV), C-O (285.8 eV), and C=O (288.8 eV). These oxygen-containing groups could improve the wettability of the electrolytes, resulting in enhanced accessibility of ions to more surface area to yield increased specific capacitances [24, 25]. The dynamic water contact angle measurement of Fig. 3e revealed an initial contact angle of 97° for the AC-4 electrode but vanished after 5 min. By contrast, the commercial AC was very hydrophobic to yield an initial contact angle of 129° that remained at 74° after 5 min (Fig. 3f).

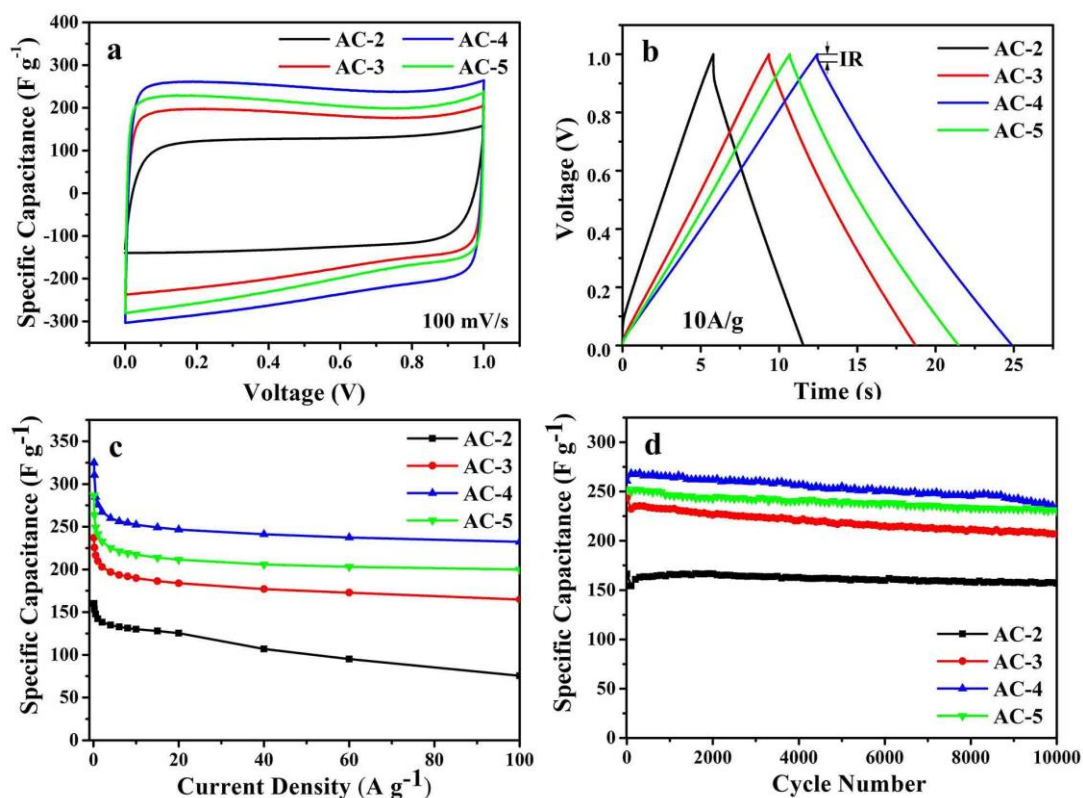


**Figure 4.** Electrochemical measurements of all samples: CV curves of ACs at 100  $\text{mV s}^{-1}$  (a), GCD curves at 10  $\text{A g}^{-1}$  (b), charge/discharge rate performance (c), and cycle life at 1  $\text{A g}^{-1}$  (d).

The CV curves of the ACs samples at  $100 \text{ mV s}^{-1}$  scan rate are presented in Fig. 4a. All the curves roughly displayed similar rectangular shapes, indicating an ideal EDLC behavior. The specific capacitances calculated from the CV curves were 122, 183, 235 and  $211 \text{ F g}^{-1}$  for AC-2, AC-3, AC-4 and AC-5, respectively. The symmetrical straight-lined GCD curves of Fig. 4b also indicated typical EDLC characteristics. An elevated specific capacitance reaching up to  $244 \text{ F g}^{-1}$  at a current density of  $10 \text{ A g}^{-1}$  was obtained with the AC-4. Meanwhile, a lower internal resistance (IR) drop of 14 mV was recorded with AC-4 if compared to AC-2. This indicated a higher power density, which was consistent with the rate performance (Fig. 4c). As the current density increased, the capacitance change for AC-3, AC-4 and AC-5 followed similar trends, while a sharp decrease was noticed with AC-2 at high current densities (only  $76 \text{ F g}^{-1}$  at  $100 \text{ A g}^{-1}$  was recorded). This suggested that mesopores structure are favorable for fast ions transfer at elevated current densities [11, 26]. Thus, it might be concluded that AC-3, AC-4, and AC-5 had better electrochemical performances than AC-2. The sample AC-4 delivered a high specific capacitance of respectively 325 and  $232 \text{ F g}^{-1}$  at 0.1 and  $100 \text{ A g}^{-1}$ , with 71% capacitance retention. On the other hand, though  $V_{\text{mes}}/V_{\text{total}}$  for AC-5 was high (42.8%), the mesopore increased while the SSA declined, resulting in slightly reduced capacitance ( $286 \text{ F g}^{-1}$ ). The AC-4 exhibited an excellent reversibility with ~89% capacity retention after the 10000 cycles at  $1 \text{ A g}^{-1}$  (Fig. 4d).

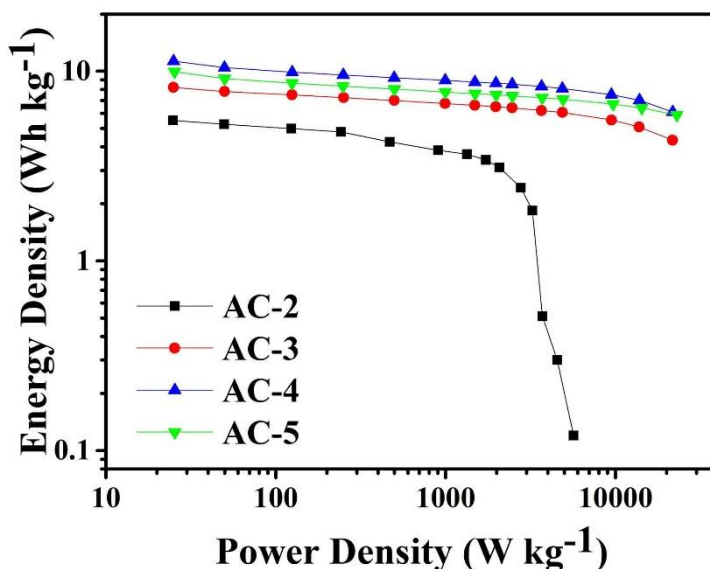


**Figure 5.** Ragone plots of ACs based supercapacitors.

The Ragone plots of Fig. 5 exhibited an outstanding performance for AC-4 in the two-electrode supercapacitor system in aqueous electrolyte. The AC-4 provided a power densities ranging from  $25 \text{ W kg}^{-1}$  to  $21.75 \text{ kW kg}^{-1}$ , corresponding to energy densities varying from  $11.28 \text{ Wh kg}^{-1}$  to  $6.11 \text{ Wh kg}^{-1}$ . The energy density of AC-2, on the other hand, deteriorated rapidly at high power density due to the lack of mesopores.

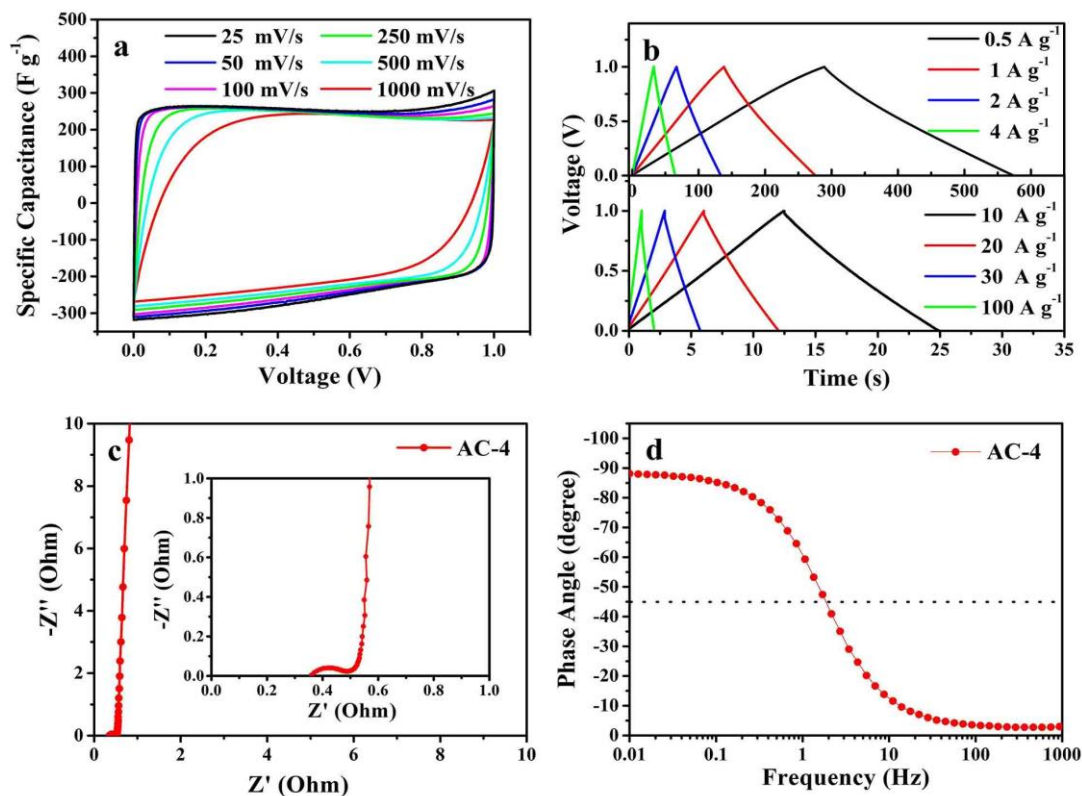


**Figure 6.** Electrochemical performance of AC-4 measured in 6 M KOH aqueous electrolyte. CV curves of AC-4 at various scan rates (a), GCD curves at different current densities (b), Nyquist plot (c), and the Bode plot (d).

Fig. 6a depicts the CV curves of AC-4 in 6 M KOH electrolyte at scan rates varying from 25 to  $1000 \text{ mV s}^{-1}$ . A perfect rectangular shape was obtained at a scan rate of  $50 \text{ mV s}^{-1}$  and even at the high scan rates of  $1000 \text{ mV s}^{-1}$ , the electrode maintained the quasi-rectangular shape. Meanwhile, all the GCD curves looked highly symmetrical at various current densities between 0.5 to  $100 \text{ A g}^{-1}$  (Fig. 6b). Hence, both the CV and charge-discharge results indicated the ideal and excellent EDLC behavior. The recorded specific capacitances of AC-4 were respectively  $285$  and  $232 \text{ F g}^{-1}$  at current densities of 0.5 and  $100 \text{ A g}^{-1}$ , with an acceptable IR drop.

In order to determine the internal Ohmic resistance, the EIS were measured in the frequency range from 100 kHz to 10 mHz (Fig. 6c). In the high-frequency region, the AC-4 electrodes exhibited a very small semicircle (inset of Fig. 6c). The point of intersection between the Nyquist plots and real axis correspond to the ESR [6], which was measured as only  $0.36 \Omega$ . In the medium frequency region, the slope at the  $45^\circ$  represents the Warburg resistance, which corresponds to the ion diffusion from the electrolyte to electrode materials [2]. As shown in the inset of Fig. 6c, the relatively short slash indicated a short ion diffusion distance and fast rate in the internal pore network of the electrode. In the low-frequency range, the recorded nearly vertical line to the real axis implied an ideal capacitor behavior with low diffusion resistance [27, 28]. The inverse of the characteristic frequency at the phase angle of  $45^\circ$  was time constant  $\tau$ [29] (Fig. 6d), which was measured to be only 0.54 s for AC-4. This

demonstrated that the presence of mesopores largely increased the ion diffusion rate, leading to an excellent rate performance and power density [30, 31].

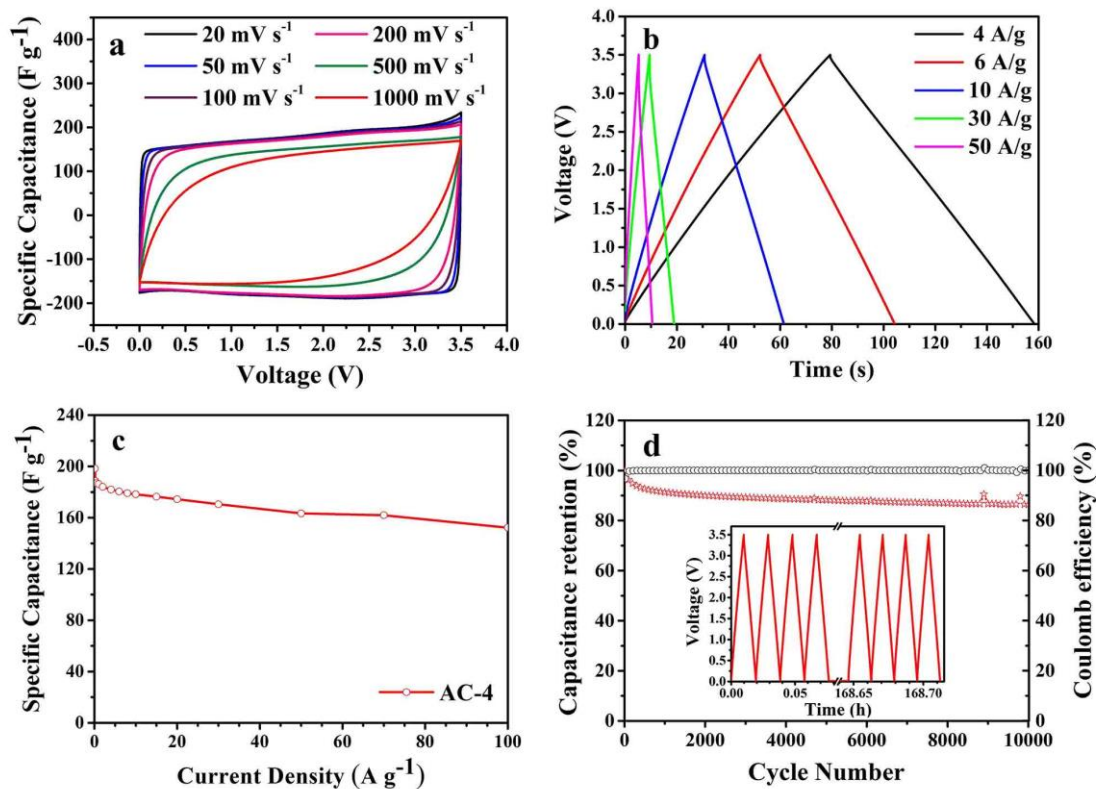


**Figure 7.** Electrochemical performance of the AC-4 in the EMIMBF<sub>4</sub> electrolyte. CV at different scan rates (a), GCD curves at various current densities (b), rate performance (c), and capacitance retention and coulomb efficiency at a current density of 10 A g<sup>-1</sup> in the EMIMBF<sub>4</sub> electrolyte (d).

In order to increase the energy density of the constructed supercapacitor, the ionic liquid (EMIMBF<sub>4</sub>), characterized by a much broader potential window, was selected as an electrolyte. The typical rectangular CV curves observed at both scan rates of 20 and 1000 mV s<sup>-1</sup> indicated the fast ions and electron transport (Fig. 7a) [32]. Also, the symmetric GCD curves recorded at various densities implied an ideal capacitive property; especially as very small IR drop at a high current density was obtained (Fig. 7b). A substantial specific capacitance up to 198 F g<sup>-1</sup> was obtained at a current density of 0.1 A g<sup>-1</sup>. Furthermore, even at an ultrahigh current density of 100 A g<sup>-1</sup>, the electrodes retained 77% of the initial capacitance to yield 152 F g<sup>-1</sup> (Fig. 7c). After 10000 cycles, the capacitance retention of AC-4 reached ~86% at 10 A g<sup>-1</sup> and the coulomb efficiency maintained nearly 100% (Fig. 7d), revealing the excellent cyclability.

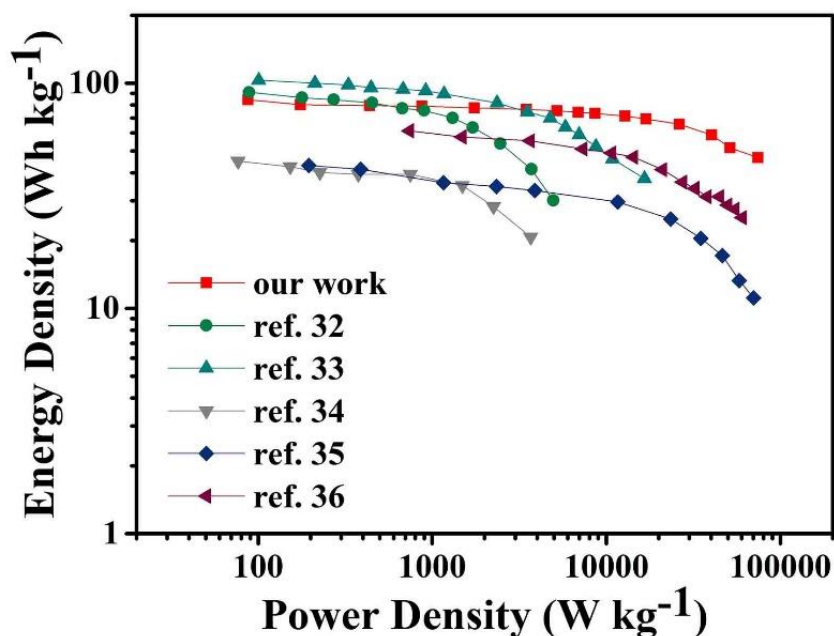


**Figure 8.** Ragone plots of AC-4 compared with biomass-derived carbon.

Compared with others biomass-derived carbon, including rice bran, silk, human hair, glucose and enteromorpha, the symmetric supercapacitors based on AC-4 exhibited a high energy density of  $84.3 \text{ Wh kg}^{-1}$  at  $87.5 \text{ W kg}^{-1}$  (Fig. 8). More importantly, the electrode retained  $46.6 \text{ Wh kg}^{-1}$  at the ultrahigh power density of  $74.2 \text{ kW kg}^{-1}$ , which was better than results of rice bran [32], silk [33], human hair [34], glucose [35] and enteromorpha [36]. The AC-4 also showed superior values than those of commercial devices (pseudocapacitor  $<30 \text{ Wh kg}^{-1}$ ) [37] and hybrid supercapacitor  $\sim 60 \text{ Wh kg}^{-1}$  [38]). The supercapacitors can fully be recharged within 2.3 s, achieving an elevated energy density of  $46.6 \text{ Wh kg}^{-1}$  under the high power density of  $74.2 \text{ kW kg}^{-1}$ . These findings showed that AC-4 is a promising electrode material for supercapacitors, especially for high power application.

#### 4. CONCLUSIONS

ACs with elevated SSA up to  $3512.83 \text{ m}^2 \text{ g}^{-1}$  and large pore volume of  $2.11 \text{ cm}^3 \text{ g}^{-1}$  was prepared from coconut shells by the low temperature carbonization and subsequent KOH activation. Both in aqueous and ionic liquid electrolytes, the AC electrodes exhibited high specific capacitances of  $325 \text{ F g}^{-1}$  in an aqueous electrolyte and  $198 \text{ F g}^{-1}$  in the ionic liquid electrolyte, with outstanding rate capability and long cycle life. Furthermore, the supercapacitors displayed excellent energy-power output properties at ultrahigh power densities. These findings illustrated that the coconut shell-based AC prepared through a cost-effective and facile method is promising for high-power and renewable energy storage devices.

## ACKNOWLEDGEMENTS

This study was financially supported by the National Natural Science Foundation of China (No: 51162006, 51362009), international S&T cooperation program of Hainan province (KJHZ2015-02) and key programs of Hainan province (ZDXM2015118).

## References

1. P. Simon, Y. Gogotsi, *Nat. Mater.*, 7 (2008) 845-854.
2. G. Wang, L. Zhang, J. Zhang, *Chem. Soc. Rev.*, 41 (2012) 797-828.
3. L.L. Zhang, X.S. Zhao, *Chem. Soc. Rev.*, 38 (2009) 2520-2531.
4. J. Liu, J.G. Zhang, Z. Yang, J.P. Lemmon, C. Imhoff, G.L. Graff, L. Li, J. Hu, C. Wang, J. Xiao, *Adv. Funct. Mater.*, 23 (2013) 929-946.
5. Y. Dai, H. Jiang, Y. Hu, Y. Fu, C. Li, *Ind. Eng. Chem. Res.*, 53 (2014) 3125-3130.
6. Y. Gao, W. Zhang, Q. Yue, B. Gao, Y. Sun, J. Kong, P. Zhao, *J. Power Sources*, 270 (2014) 403-410.
7. J. Chmiola, G. Yushin, Y. Gogotsi, C. Portet, P. Simon, P.L. Taberna, *Science*, 313 (2006) 1760-1763.
8. A. Pandolfo, A. Hollenkamp, *J. Power Sources*, 157 (2006) 11-27.
9. J. Huang, B.G. Sumpter, V. Meunier, *Angew. Chem. Int. Edit.*, 47 (2008) 520-524.
10. T.E. Rufford, D. Hulicova-Jurcakova, Z. Zhu, G. Lu, *J. Phys. Chem. C*, 113 (2009) 19335-19343.
11. H. Jiang, P.S. Lee, C. Li, *Energy Environ. Sci.*, 6 (2013) 41-53.
12. T. Panja, D. Bhattacharjya, J. Yu, *J. Mater. Chem. A*, 3 (2015) 18001-18009.
13. W. Su, L. Zhou, Y. Zhou, *Carbon*, 41 (2003) 861-863.
14. M. Galinski, K. Babel, K. Jurewicz, *J. Power Sources*, 228 (2013) 83-88.
15. L. Sun, C. Tian, M. Li, X. Meng, L. Wang, R. Wang, J. Yin, H. Fu, *J. Mater. Chem. A*, 1 (2013) 6462.
16. J. Mi, X.R. Wang, R.J. Fan, W.H. Qu, W.C. Li, *Energy Fuel*, 26 (2012) 5321-5329.
17. W. Heschel, E. Klose, *Fuel*, 74 (1995) 1786-1791.
18. J. Zhao, H. Lai, Z. Lyu, Y. Jiang, K. Xie, X. Wang, Q. Wu, L. Yang, Z. Jin, Y. Ma, J. Liu, Z. Hu, *Adv. Mater.*, 27 (2015) 3541-3545.
19. J. Yin, D. Zhang, J. Zhao, X. Wang, H. Zhu, C. Wang, *Electrochim. Acta*, 136 (2014) 504-512.
20. D. Kang, Q. Liu, J. Gu, Y. Su, W. Zhang, D. Zhang, *ACS Nano*, 9 (2015) 11225-11233.
21. V. Zolyomi, J. Koltai, J. Kirti, *Phys. Status Solidi B*, 248 (2011) 2435-2444.
22. Z. Li, Z. Xu, X. Tan, H. Wang, C.M. Holt, T. Stephenson, B.C. Olsen, D. Mitlin, *Energy Environ. Sci.*, 6 (2013) 871-878.
23. K. Wang, N. Zhao, S. Lei, R. Yan, X. Tian, J. Wang, Y. Song, D. Xu, Q. Guo, L. Liu, *Electrochim. Acta*, 166 (2015) 1-11.
24. V. Ruiz, C. Blanco, E. Raymundo Piñero, V. Khomenko, F. Béguin, R. Santamaría, *Electrochim. Acta*, 52 (2007) 4969-4973.
25. M.J. Bleda Martínez, J.A. Maciá Agulló, D. Lozano Castelló, E. Morallón, D. Cazorla Amorós, A. Linares-Solano, *Carbon*, 43 (2005) 2677-2684.
26. D.W. Wang, F. Li, M. Liu, G. Lu, H.M. Cheng, *Angew. Chem. Int. Edit.*, 120 (2008) 379-382.
27. H. Liu, P. He, Z. Li, Y. Liu, J. Li, *Electrochim. Acta*, 51 (2006) 1925-1931.
28. E. Frackowiak, F. Béguin, *Carbon*, 39 (2001) 937-950.
29. X. Yang, C. Cheng, Y. Wang, L. Qiu, D. Li, *Science*, 341 (2013) 534-537.
30. M.F. El-Kady, V. Strong, S. Dubin, R.B. Kaner, *Science*, 335 (2012) 1326-1330.
31. Y. Xu, Z. Lin, X. Zhong, X. Huang, N.O. Weiss, Y. Huang, X. Duan, *Nat. Commun.*, 5 (2014).
32. J. Hou, C. Cao, X. Ma, F. Idrees, B. Xu, X. Hao, W. Lin, *Sci. Rep.*, 4 (2014) 7260.
33. J.H. Hou, C.B. Cao, F. Idrees, X. Ma, *ACS Nano*, 9 (2015) 2556-2564.

34. W. Qian, F. Sun, Y. Xu, L. Qiu, C. Liu, S. Wang, F. Yan, *Energy Environ. Sci.*, 7 (2014) 379-386.
35. T. Tooming, T. Thomberg, H. Kurig, A. Jänes, E. Lust, *J. Power Sources*, 280 (2015) 667-677.
36. W. Yu, H. Wang, S. Liu, N. Mao, X. Liu, J. Shi, W. Liu, S. Chen, X. Wang, *J. Mater. Chem. A*, (2016).
37. M. Sevilla, R. Mokaya, *Energy Environ. Sci.*, 7 (2014) 1250.
38. Y. Ma, H. Chang, M. Zhang, Y. Chen, *Adv. Mater.*, 27 (2015) 5296-5308.

© 2016 The Authors. Published by ESG ([www.electrochemsci.org](http://www.electrochemsci.org)). This article is an open access article distributed under the terms and conditions of the Creative Commons Attribution license (<http://creativecommons.org/licenses/by/4.0/>).